Buzolin, R.H.; Mendis, C.L.; Tolnai, D.; Stark, A.; Schell, N.; Pinto, H.; Kainer, K.U.; Hort, N.:

In situ synchrotron radiation diffraction investigation of the compression behaviour at 350 °C of ZK40 alloys with addition of CaO and Y

In: Materials Science and Engineering A (2016) Elsevier

DOI: 10.1016/j.msea.2016.03.121

In situ synchrotron radiation diffraction investigation of the compression behaviour at 350 °C of ZK40 alloys with addition of CaO and Y

R. H. Buzolin[1,2] and C. L. Mendis[1], D. Tolnai[1], A. Stark[1], N. Schell[1], H. Pinto[2], K. U. Kainer[1], N. Hort[1]

[1]Institute of Materials Research, Helmholtz-Zentrum Geesthacht, Geesthacht, Germany
[2]Department of Material Engineering, University of São Paulo, Av. Jão Dagnone, 1100 Jd. Sta Angelina, 13563-120 São Carlos, Brazil

Abstract

The evolution of the microstructure during compression is investigated with in situ synchrotron radiation diffraction in as-cast ZK40, ZK40-2CaO and ZK40-1Y Mg alloys. The specimens were compressed at 350 °C with a strain rate of 10^3 s^{-1} until 30% deformation. The Y containing alloy showed the highest 0.2% proof strength in compression of 35 MPa at 350 °C which is double that of the ZK40 alloy, while the CaO added alloy shows a moderate increment at 23 MPa. The Y containing alloy shows some work hardening, while the CaO modified and the ZK40 alloys do not show work hardening after yield. Synchrotron radiation diffraction timelines show that continuous and discontinuous dynamic recrystallization occurs during deformation of the ZK40 alloy while a small amount of dynamic recrystallization was observed in the ZK40-1Y alloy. However, dynamic recrystallization was not present in the ZK40-2CaO alloy. SEM-EBSD analysis conducted on the deformed samples shows a significantly high volume fraction of twins in the Y and CaO containing alloys which was absent in the ZK40 alloy. The modified deformation behaviours observed in the CaO and Y containing alloys were attributed to the presence of intermetallic particles found at the grain boundaries and to the role of Ca and Y in stabilising twinning.

1 Introduction

The high specific strength [1] of Mg alloys, makes these alloys attractive for potential applications where weight reduction is of importance. Thus, research and development of Mg alloys for possible industrial applications have increased recently [2–4]. Conventional Mg alloys exhibit poor formability at room temperature [5], thus the mechanical processing is done at higher temperatures (> 225 °C) to activate non-basal slip and to reduce twinning [6]. The deformation behaviour and dynamic recrystallization of Mg alloys have been investigated thoroughly [7– 9] and several dynamic recrystallization mechanisms at different temperatures have been reported [10–12].

Alloys based on the Mg-Zn system are low in cost and have relatively good mechanical properties [13]. The ZK60 (Mg-6.0Zn0.6Zr (wt%)) alloy is a commercially available wrought Mg alloy which shows a good combination of strength and ductility. Recently, there are numerous attempts to enhance the strength and ductility through the modification of alloy chemistry with the addition of quaternary and quinary additions [14–15]. Wu et al. [16] investigated the compression behaviour of the ZK60 alloy at different temperatures and found that the range between 250 °C and 350 °C was the most suitable to deform this alloy.

The role of Ca additions on the microstructure modification [17,18], mechanical properties [19,20] and texture randomisation [17,21,22] has been reported in literature for both commercial and experimental magnesium alloys. It has been shown that the Ca additions alone improved the ignition resistance [23] of Mg alloys. Recently the addition of CaO was found to improve the ignition resistance of Mg alloys [24], and CaO reduces to form MgO and Mg_2Ca [25] providing an easier route to add Ca to Mg alloys. The addition of Ca to ZK series alloys lead to the refinement of the rod like β_1 and plate like β_2 precipitates and enhanced the creep resistance [26]. The Mg-Zn-Ca system was investigated with different Zn contents by Oh-ishi et al. [25]. It was found that a Ca:Zn ratio of $\sim$ 1:3 (wt%) shows the best enhancement in age hardening which can be further enhanced by the addition of Nd [27]. Additionally, the cast and heat treated Mg-Ca-Zn alloys show enhanced creep resistance both in tension [27] and compression [28]. The extruded and hot rolled Mg-Zn-Zr alloys containing Ca show enhancement in mechanical properties and the modification of the strong basal texture gives rise to a weaker texture [21]. The elevated temperature deformation of Ca containing Mg alloys shows that Ca plays an important role in elevated temperature deformation of Mg based alloys [17,18,29]. However, the exact role of Ca additions during hot deformation of Mg alloys, especially in Mg-Zn-Zr based alloys, remains unclear.

The role of Y in Mg based alloys has been studied extensively. The microstructure and mechanical properties of Mg-Zn based alloys are modified by the addition of Y depending on the ratio of Y/Zn. When this ratio is large, i.e. Y rich

alloys containing Zn, then fine scaled LPSO (long period stacking ordered) structures are observed [30]. With intermediate ratios of Y/Zn, [31,32] Y modified the grain boundary phases for icosahedral phases containing Y and Zn. In the extruded alloys containing icosahedral phase a reduction in the yield anisotropy between compressive and tensile yield strengths was observed [31], and the increased strength was attributed to increased load transfer between the matrix and the second phase [33]. The addition of Y to Mg-Zn alloys shows enhanced tensile yield strength and ultimate tensile strength without significant loss in ductility [34]. Farzadfar et al. [35] found that in Mg-Zn-Y-Zr alloys did not show texture randomisation following hot compression and annealing unlike the binary Mg-Y alloys. However this is not consistent with other observations by Xu et al. [32].

Additionally, the retardation of recrystallization was observed in Mg-Y alloys which were not observed in Mg-Zn-Y alloys following hot deformation and annealing [35]. In binary Mg-Y alloys, Y accommodates the c-axis deformation through accelerating the c + a axis glide [36], which weakens the deformation anisotropy and thus improves ductility. Transmission Electron Microscopy (TEM) experiments and Density Functional Theory (DFT) calculations suggested that the addition of Y to Mg alloys results in the decrease of the intrinsic stacking fault energy (SFE) leading to the subsequent promotion of the $\langle c + a \rangle$ slip [37]. Recent investigations with in situ neutron diffraction show that the solute strengthening effect of Y which increased the critically resolved shear stresses (CRSS) for basal slip, $\langle a+c \rangle$ slip and twinning compared with pure Mg, with basal slip showing the smallest increment in hardening [38]. The increased ductility observed was due to the accommodation of strain by grains in softer orientations during deformation [38]. Even though there is a significant collection of work on the effect of Y additions to Mg and Mg-Zn-Zr alloys there are some discrepancies the observations associated with hot deformation and microstructure evolution.

X-ray and neutron diffraction are well established characterization methods to investigate the structure of various crystalline materials. Recently, it became possible to perform these measurements in situ which allow detection of the dynamic microstructural processes that occur during mechanical loading in real time [39–47]. The azimuthal angle-time plots (AT-plots) give information on grain size evolution, grain rotation, texture evolution, strain and strain anisotropy, that can be correlated with dislocation slip, sub-grain formation, twinning, recovery, recrystallization and grain growth, which are the physical processes responsible for the microstructural changes [39].

Using in situ synchrotron radiation diffraction during compression testing the formation and the propagation of twins, grain rotation and the formation of recrystallized grains may be observed. These provide a real time insight into the processes that contribute to the evolution of microstructure during deformation, especially at elevated temperatures where many dynamic processes, such as re-

Table 1: Actual chemical compositions of the alloys investigated.

Alloy	Ca	Y	Zn	Zr
ZK40	-	-	5.00	0.53
ZK40-2CaO	1.00	-	4.30	0.55
ZK40-1Y	-	1.15	4.00	0.40

covery and recrystallization, contribute to the deformation. As these observations are made in parallel to deformation step, the global strains required for each of these events to occur may be elucidated at a given temperature and strain rate. It is well known that during elevated temperature deformation a number of competing processes such as twinning, dislocation motion and recovery and recrystallization take place. With the aid of in situ experiments an understanding of which of these modes control the deformation at different parts of a deformation curve may be understood. It is envisaged that understanding of the contributions from various deformation modes available at the elevated temperature though in situ investigation of microstructure evolution during deformation will a rudimentary insight into more complex deformation processes that occur during thermos-mechanical treatments.

The aim of this study is to investigate the influence of CaO and Y addition on the elevated temperature deformation at 350 °Cof ZK40 alloy with in situ synchrotron radiation diffraction, which provides new insights into the real-time evolution of the microstructure. The results are correlated with post mortem electron backscattered diffraction (EBSD), which provides information on the deformed microstructures.

2 Experimental procedures

The alloys were produced by permanent mould indirect chill casting [48]. Mg was molten under protective gas (98 vol% Ar, 2 vol% SF_6) in an electric resistance furnace. Zn and CaO were added to the melt in the pure form, while Y was added as Mg10 wt% Y and the Zr as Zirmaxs alloy (Mg-33 wt% Zr). After mixing, the melt was poured into a preheated (660 °C) thin walled steel mould at a temperature of 750 °C. The mould was then held at 660 °C for 15 min before immersing into water at 10 mm s^{-1} until the top of the melt was in line with the cooling water. Actual composition of the alloys investigated are provided in Table 1.

The samples were mounted in epoxy and ground using SiC paper, then polished using 3 mm diamond suspension followed by OPS solution with 1 mm diamond suspension as the last step of polishing. The microstructures for opti-

cal microscopy (OM) were etched with an acetic-picric solution [5]. The optical microscopic analysis was performed using a Leica DMI 5000 light optical microscope. The grain sizes were measured using methods described in ASTM standard E112-13 [49] using a minimum of 5 images.

The specimens for EBSD were unetched but washed with 0.5 vol% nitric acid in ethanol solution for 5 s and then washed with ethanol to remove any trace of the nitric acid. The scanning electron microscopy (SEM) investigation was performed using a Zeiss FEGSEM Ultra 55 microscope equipped with a Hikari detector and a TSL-OIM software package for EBSD analysis. The EBSD measurements on the compressed samples were performed on an area 80 mm x 80 mm, with a step size of 0.1 mm close to the centre of the deformed specimen to ensure a similar area to that of those samples measured during the diffraction experiment. The minimum grain size was chosen to be 10 mm with a confidence index of 0.09. All microstructures of deformed samples are presented so that the compression direction is parallel to the horizontal direction of the page.

The in situ synchrotron radiation diffraction experiments were performed at the P07 beamline of PETRA III, DESY (Deutsches Elektronen-Synchrotron). A monochromatic beam with the energy of 100 keV (λ = 0.0124 nm) with a cross section of 1.0 x 1.0 mm^2 was used for the current investigation. For the in situ compression experiments cylindrical specimens were machined from the cast ingots with a diameter of 5 mm and a length of 10 mm. The diffraction patterns were recorded with a PerkinElmer 1622 flat panel detector with a pixel size of 200 x 200 mm^2, which was placed at a sample-to-detector distance of 1535 mm from the specimen (distance was calibrated with a LaB_6 standard powder sample). The acquisition time for each image was 1 s. The specimens were placed in the chamber of a DIL 805 A/D dilatometer (TA Instruments, Hüllhorst, Germany), combined with a modified heating induction coil so the beam passes only through the sample [50]. The specimens were heated to 350 °C at a rate of 30 K s^{-1} and held at this temperature for 3 min before the deformation to ensure temperature homogeneity. The specimens were compressed with an initial strain rate of 1.1 x 10^3 s^{-1}. The tests were terminated at a total strain of 0.3.

The morphology of the Debye-Scherrer rings was then analysed using the Fit2Ds software and converted into azimuthal-angle time (AT) plots using the ImageJs software package. The two dimensional diffraction patterns were radially transformed into azimuthal angle – 2Θ plots, by stacking sections of the plots acquired through the measurement at a given 2Θ angle which is attributed to reflections originating from the chosen crystallographic plane which is used to construct the azimuthal-angle time (deformation) plots. The time measured may be correlated with the applied true strain as each diffraction pattern was recorded at a specific strain through the measurement.

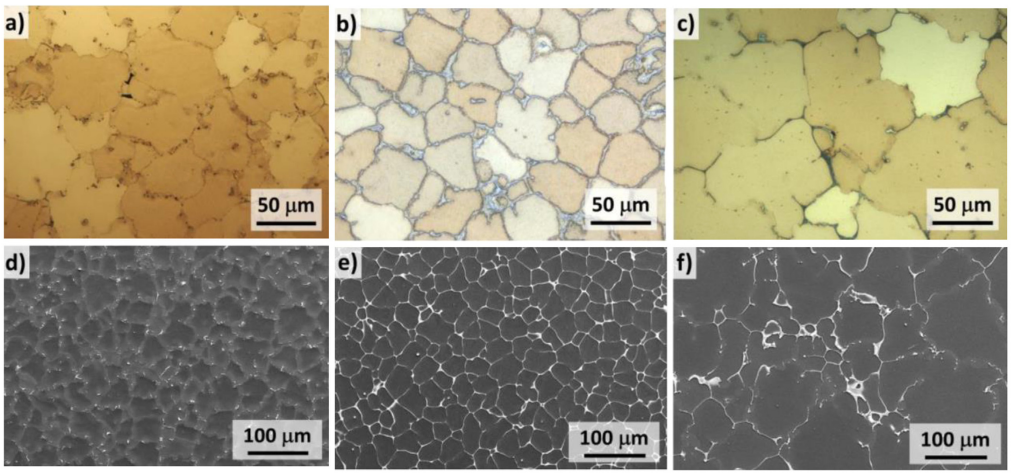

Figure 1: (a-c) Optical and (d-f) SEM micrographs of as-cast ZK40 (a, d), ZK40-2CaO (b, e), and ZK40-1Y (c, f).

3 Results

The optical micrographs and SEM images of the as-cast ZK40, ZK40-2CaO and ZK40-1Y alloys are shown in Fig. 1. The grain size of ZK40 was evaluated to be 72.43 $\pm$ 2.55 mm, for ZK40-2CaO 75.94 $\pm$ 5 mm, while for ZK40-Y a grain size of 86.06 7 4.53 mmwas measured. The intermetallic phases were distributed semi-continuously along the grain boundaries in the ZK40-2CaO and ZK40-1Y alloys, whereas the unmodified ZK40 alloy contained discrete intermetallic particles along the grain boundaries, Fig. 1 (d-f). All investigated alloys exhibit a cellular microstructure in the as-cast condition.

The true stress–true strain curves from the in situ compression experiments are shown in Fig. 2. A 0.2% compressive proof strength ($\sigma_{0.2}$) was measured to be 17 MPa in ZK40 alloy, while the maximum stress (σ_{max}) was 26.5 MPa. In the ZK40-2CaO a $\sigma_{0.2}$ of 23.3 MPa was observed which followed a decrease in the true stress. The ZK40-1Y alloy exhibited the highest 0.2% compressive proof strength, at 35 MPa, and a maximum compressive stress of 65.6 MPa. The ZK40-1Y alloy shows work hardening following yield while ZK40 and ZK40-2CaO alloys do not, in fact ZK40-2CaO shows softening after the yield.

The AT-plots of the $\{10\bar{1}0\}$ planes and the $\{0002\}$ planes from the in situ synchrotron radiation diffraction measurements illustrating the deformation are plotted in Fig. 3. During the initial stages of deformation, i.e. in the elastic regime, the diffraction patterns did not change significantly. The blurring of the timelines, i.e. the trace of a given reflection over deformation can be observed in region I of Fig. 3(a) for ZK40 alloy. In the plastic deformation regime a tendency

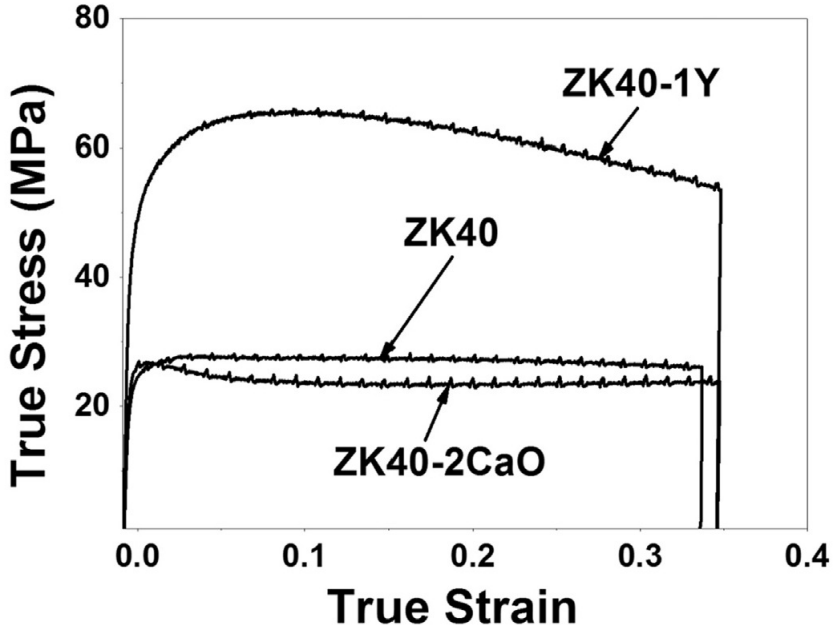

Figure 2: True stress–true strain curves obtained during compression at 350 °C.

of broadening of the reflections and merging of timelines to develop the final texture of the material can be observed (II), as shown in Fig. 3(a). Region III shows inclination of the timelines, which is attributed to grain rotation. During plastic deformation new timelines appear from blurred regions, in region IV in Fig. 3(a), which is attributed to the formation of recrystallized grains.

Regions V and VI in Fig. 3(b) show blurred regions due to the sub-grain formation for the ZK40-2CaO alloy. In region VII of Fig. 3 (c) the appearance of timelines was observed at the start of the plastic deformation and these timelines continue to remain through the deformation. Regions showing the appearance of new timelines associated with recrystallization could be observed in the ZK40-1Y alloy in the later stages of deformation.

The optical micrographs of the deformed samples are shown in Fig. 4. Twins were seldom observed in the ZK40 alloy while the ZK40-2CaO and ZK40-1Y alloys both contain a significant fraction of twins distributed through the microstructure. The number density of twins is higher in the CaO modified alloy compared with the Y modified alloy.

The EBSD inverse pole figure (IPF) maps of the compressed samples are shown in Fig. 5(a-c). The corresponding KAM (Kernel average misorientation) maps for each alloy corresponding to the IPF are illustrated in Fig. 5(d-f). The ZK40 alloy, Fig. 5(a and d), contain recrystallized grains along grain boundaries, which correspond to regions with low misorientations on the KAM maps, and an

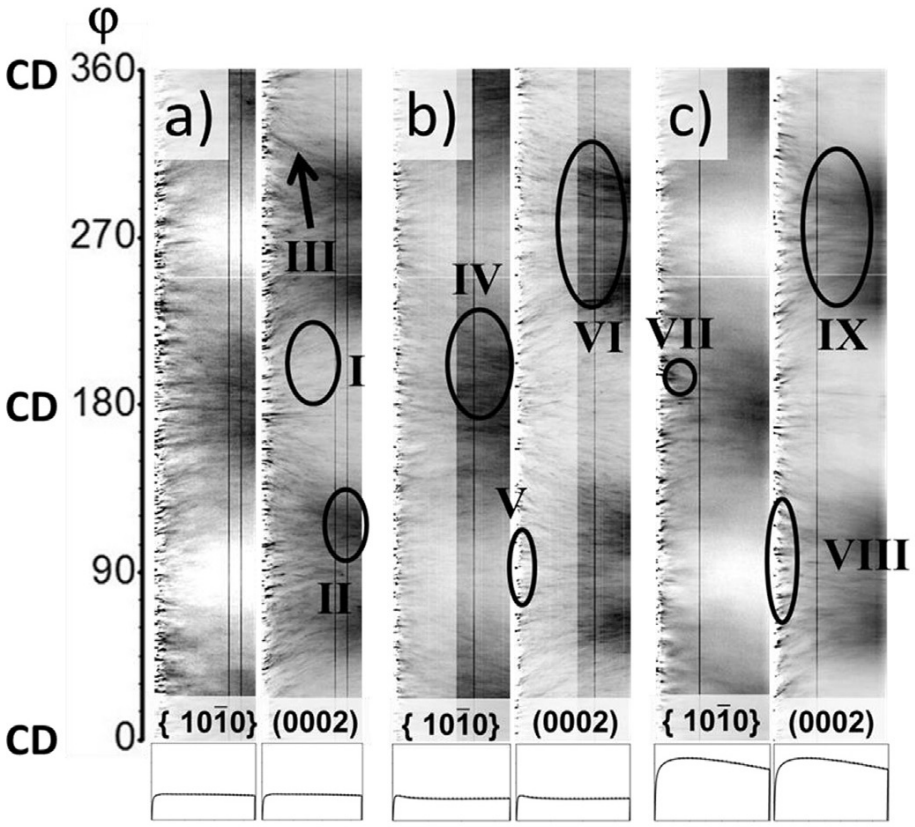

Figure 3: Azimuth angle vs timeplots obtained during in situ synchrotron radiation diffraction during compressive deformation of (a) ZK40, (b) ZK40-2CaO and (c) ZK40-1Y alloys. CD represents the compression direction.

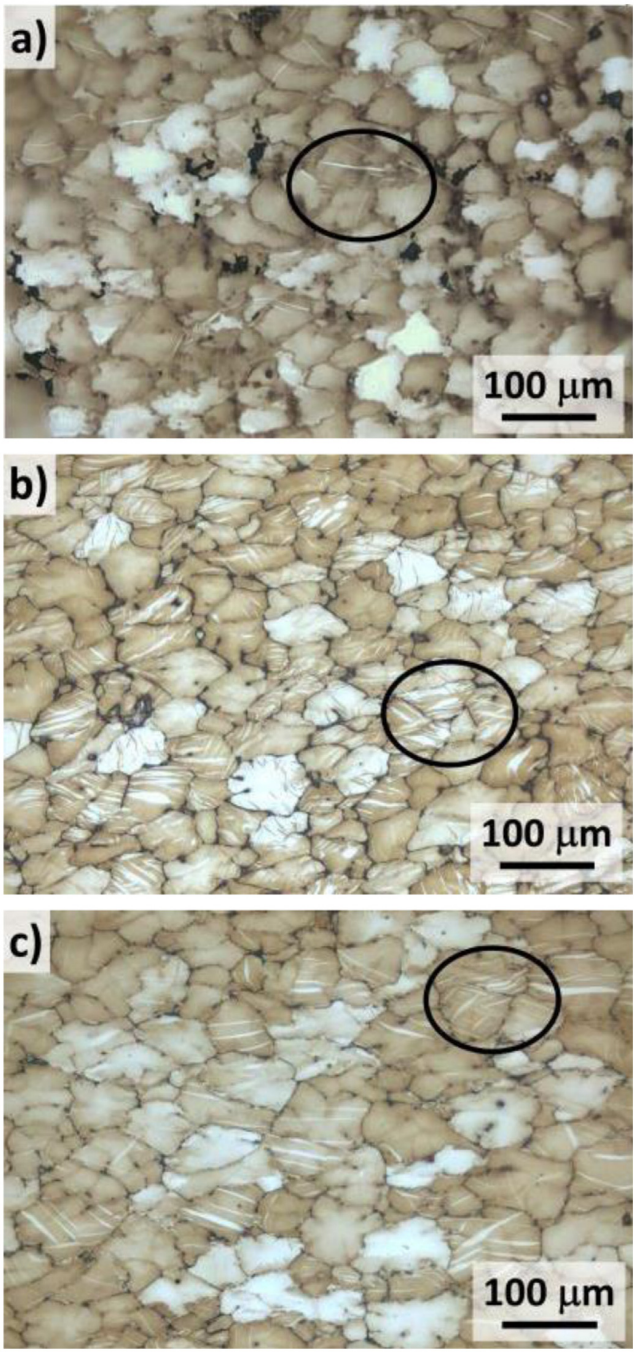

Figure 4: Optical microstructure of samples after a total compressive strain of 30% at 350 °C (a) ZK40, (b) ZK40-2CaO, and (c) ZK40-1Y.

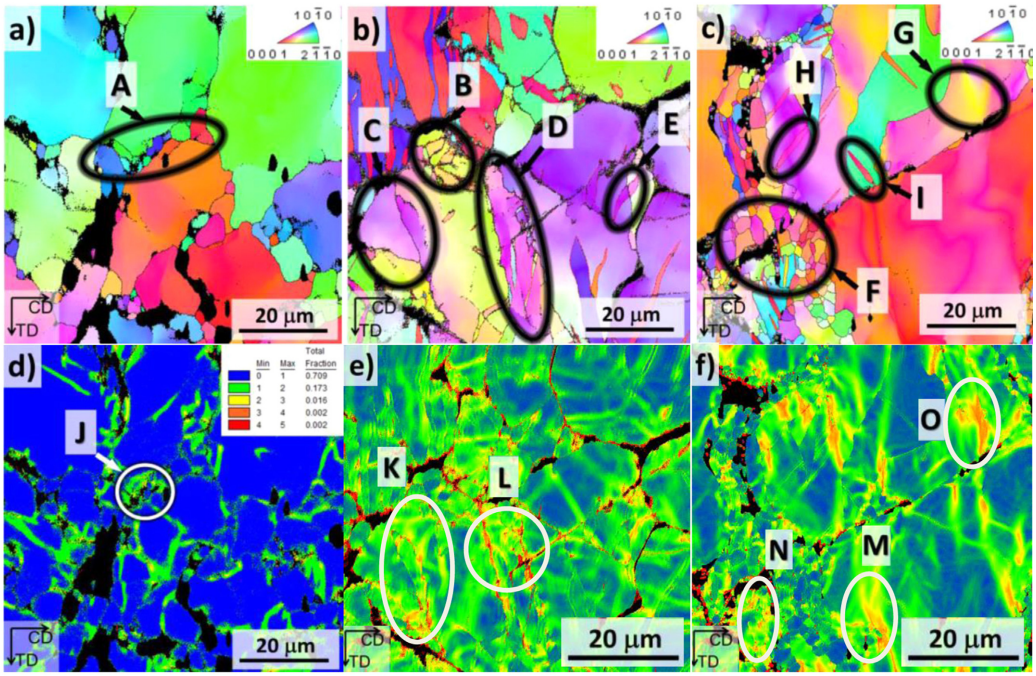

Figure 5: EBSD inverse pole figure maps (a-c) and Kernel average misorientation angle maps (d-f) for the samples subjected to a total compressive strain of 30% at 350 °C (a,d) ZK40, (b,e) ZK40-2CaO, and (c,f) ZK40-1Y.

example of recrystallized grains is shown in Region A in Fig. 5(a). Additionally, there are regions within grains which have slightly different misorientations, as shown in Region B. In KAM maps these regions correspond to regions with low misorientations bound by lines with an angle of misorientation between 1° and 2°, and such regions can be described as sub grains. Generally, ZK40 alloy did not contain regions where the misorientation within the grains was more than 2°.

The ZK40-2CaO alloy contained many regions where the misorientation within the grain was relatively large, Fig. 5(b) and (e). There is no evidence of recrystallization in the regions examined in ZK40-2CaO alloy. The ZK40-2CaO alloy contained a large density of twins and sub grains as indicated by regions B, C and D, respectively, Fig. 5(b). The corresponding KAM map, in Fig. 5(e), shows that in the area corresponding to region D in Fig. 5(b) there are sub grain boundaries containing a higher misorientation angle with the nearest neighbour than that observed within the grains.

The twin observed in region D contains regions of high misorientation within indicative of sub grain formation. The ZK40-1Y alloy behaved in a manner similar to the ZK40-2CaO alloy with significant number density of twins (e.g. region E) and sub grains (region F), Fig. 5(c). However, unlike ZK40-2CaO, ZK40-1Y also contained recrystallized grains (region G), Fig. 5(c). The areas, in Fig. 5(f), corresponding to the regions containing sub-grains, on Fig. 5(c), contain walls of high misorientation within grains inside, with only negligible amount of misorientation. The recrystallized grains are identified as grains where there is a misorientation of $\sim 10^{\circ}$ or more between the grains, but there is no large scale misorientation within the grains. The SEM micrographs of the deformed ZK40, ZK40-2CaO, and ZK40-1Y alloys are shown in Fig. 6. The red circles highlight the areas where intermetallic particles seem to fracture. The micrographs of the samples prior to deformation did not contain fractured particles along the grain boundaries.

4 Discussion

The modified alloys contain semi-continuously distributed intermetallic particles along the grain boundaries, and content of Y and Ca in solution is not significant. CaO was not observed in the final microstructure, only intermetallic compounds containing Ca, as reported previously by Wiese et al. [24] CaO disassociates during melting and solidification. Apart from slight differences of Zn content, the matrix is similar between the alloys. Therefore, the different compression behaviours exhibited among the alloys in the present study is likely to be due to the intermetallic compounds along the grain boundaries and possible differences in solute content in Mg matrix. The maximum compressive strength of the ZK40-

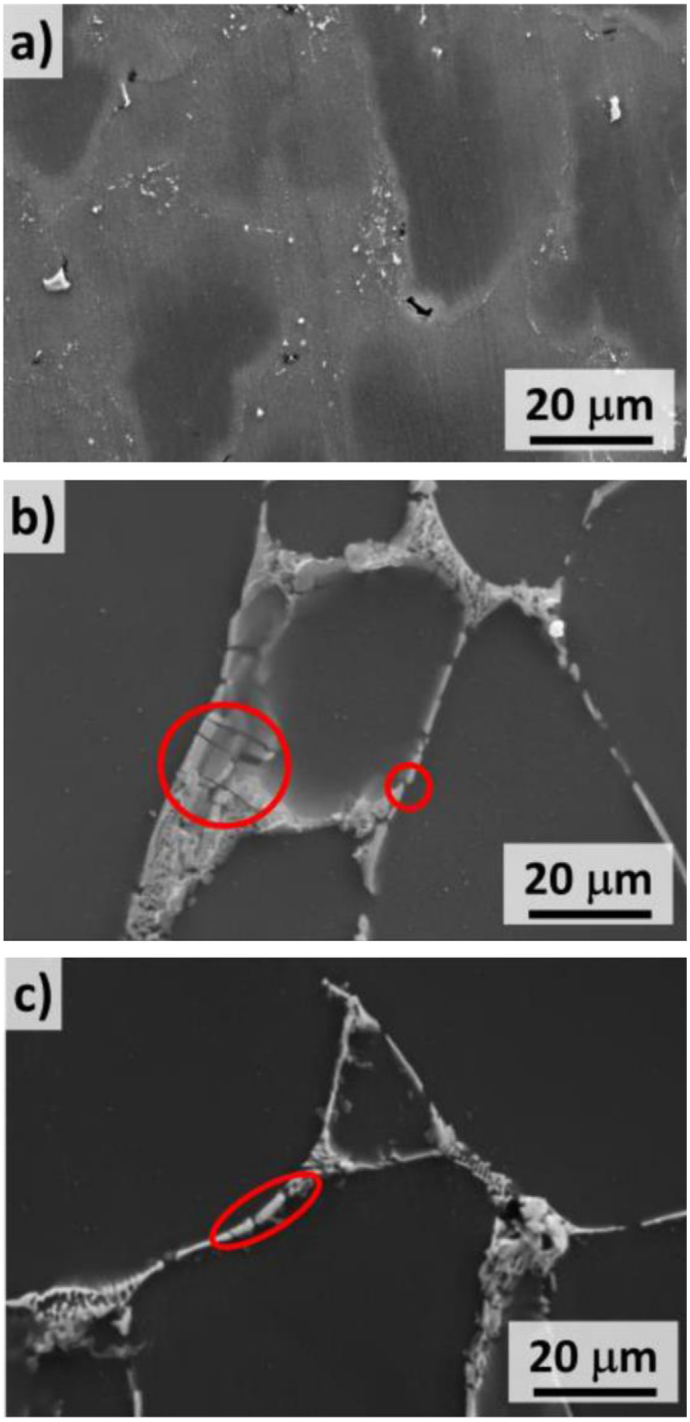

Figure 6: SEM micrographs of the samples deformed to a total stain of 30% in compression showing cracks in intermetallic particles (a) ZK40, (b) ZK40-2CaO, and (c) ZK40-1Y.

2CaO alloy was lower than the ZK40 alloy even though the yield strength of the alloy was slightly higher, suggesting that the intermetallic particles containing Ca were not effective in preventing deformation along grain boundaries, i.e. the Ca containing intermetallic particles did not contribute to work hardening of the alloy.

The strengthening caused by the presence of the Y containing compounds along the grain boundary, on the other hand, was pronounced. The flow curves show that yield strength and maximum compressive strength of ZK40-1Y were the highest among the studied alloys. As illustrated in Fig. 6, the deformed specimens exhibit cleavage of the intermetallic compounds in ZK40-2CaO and ZK40-1Y, evidencing the reinforcement effect that led to an increment of the yield strength observed during deformation at 350 °C in the ZK40-1Y alloy, i.e. the stress required to deform and consequently break the Y containing compounds is much higher than those in the ZK40 alloy. The softening behaviour subsequent to yielding observed in the CaO and Y containing alloys attributed to the cleavage of these intermetallic particles, as a significant softening behaviour is not observed in ZK40 alloy.

There are three mechanisms of dynamic recrystallization (DRX) operative: continuous dynamic recrystallization in Mg alloy, discontinuous dynamic recrystallization, and dynamic recrystallization associated with twinning [51]. The evolution of these mechanisms can be obtained from the AT-plots and the investigation of the deformed microstructure. These processes played important roles on the evolution of the microstructure during the compression at 350 °C for each alloy. In this way, during the initial stages of deformation no changes in the timelines are observed at the ATplots for the three investigated alloys. Entering the plastic behaviour, the diffraction timelines tend to rotate toward the compression directions in case of $\{10\bar{1}0\}$ planes, while a rotation away from the compression direction was observed for the (0002) reflections. Such events were more pronounced for the ZK40 alloy, as can be noticed in the AT-plots in region III. Such process has been observed previously during and prior to high temperature deformation by Schmoelzer et al. [42], and it is attributed to grain rotation, which occurs to accommodate strain build up within the microstructure.

The highly deformed and elongated grains of the ZK40-2CaO alloy, shown in region C in Fig. 5(b), show a grain that was possibly a sub-grain formed during the deformation, and the low-angle grain boundaries were transformed into high-angle grain boundaries through absorption of the dislocations. Therefore, these subgrains became dynamically recrystallized grains by continuous dynamic recrystallization [4]. Investigating the KAM values distribution for the same region shows that high values are exhibited in region K in Fig. 5(e), suggesting that this region is highly deformed. By blurring of the timelines in AT-plots in Fig. 3(b), region IV and region VI, it is suggested that the active recrystallization process during compression was continuous dynamic recrystallization.

In the ZK40-1Y alloy, a highly deformed microstructure is observed, Fig. 5(c) and (f), which is similar to that in ZK40-2CaO alloy. In region G in Fig. 5(c) sub grain formation is highlighted. Similarly in the KAM maps, region O in Fig. 5(f), where the misorientation value was high, indicates the presence of a large amount of sub grains. Correspondingly, in the AT-plots, Fig. 3(c), a pronounced blurring of the timelines was observed. This process was also observed in the ZK40 alloy. However, comparing the three alloys it is clear that the blurring of the timelines was less pronounced for the ZK40 alloy. Likewise, the Kernel maps in Fig. 5 (d) shows that ZK40 alloys exhibit the lowest misorientation values within the grains. In the ZK40-1Y alloy, in region F of Fig. 5(c), a significant amount of recrystallized grains are observed at the grain boundaries. The recrystallization occurs at the original grain boundaries.

The recrystallized grains grow through the migration of grain boundaries during the hot deformation process; the appearance of new timelines is shown in AT-plots (Fig. 3(c), region VII). This was not observed in the ZK40-2CaO alloy, suggesting that discontinuous dynamic recrystallization was not operative in the ZK40-2CaO alloy. This suggests that the sub-grain formation was less active in the initial stages during the ZK40-1Y alloy compared with ZK40-2CaO alloy. The KAM maps exhibit the highest values of misorientation at the sub-grain boundaries, indicating that these sites may initiate recrystallization. In ZK40-1Y alloy the particles along the grain boundaries possessed significantly higher strength than the ZK40-2CaO alloy, as was suggested by the flow curves. Therefore, these particles have hampered grain boundary sliding more efficiently and accommodate a higher stress during the compression, which was beneficial to nucleation and growth of recrystallized grains in the ZK40-1Y alloy.

In terms of the impact of twinning on the structure, once nucleated, the $\{10\bar{1}2\}$ twins grow laterally, followed by a small amount of dislocation plasticity, which relaxes the local stresses at the extremities of the twins, causing further twin growth [52]. Twin propagation and growth are responsible for the hardening and texture evolution characteristic of Mg alloys subjected to plastic deformation [53,54]. The inverse pole figure map, in Fig. 5 (b), shows three twins (regions B, D and E). A large amount of strain is observed in region L in Fig. 5(d), indicated large misorientation angles, suggesting that, although the grain has twinned, its orientation and the pinning caused by the presence of the intermetallic compounds at the grain boundary was favourable for twin nucleation. Even though such effect is not clearly visible in the AT-plots (Fig. 3(b)) due to the intensive blurring of the timelines, it is noted that at the end of the deformation there are no visible $\{10\bar{1}0\}$ planes with their reflections close to 90° or 270°.

Thus, it is expected that twins engulf grains with this orientations completely. Since no traces of discontinuous dynamic recrystallization were observed in the microstructure after deformation, the energy created during compression is re-

leased by twining and continuous dynamic recrystallization. In the same way, regions I and H of Fig. 5(f) show twins in the microstructure after compression for the ZK40-1Y alloy. In Fig. 5(f) KAM map show high values of misorientation in the regions with twins, as highlighted in region M. Pinning due to intermetallic compounds and the hindering of the grain sliding is not favourable for discontinuous recrystallization of the ZK40-1Y alloys. On the other hand, since there is no semi-continuous distribution of intermetallic compounds hampering the grain slide, and only small intermetallic particles at the grain boundaries, the grains had more freedom to deform in ZK40 alloy. Therefore, dynamic recrystallization was more pronounced for this alloy and the twinning not present in the deformed microstructure.

In ZK40-2CaO and ZK40-1Y alloys twins that form in the microstructure are stable during deformation and did not show signs of recrystallization at the twin boundaries. This suggests that the twins are stable and resistant to growth or recrystallization. Ostapovets and Gröger [55] simulated the strain along the tensile twin boundaries and found that there is an alternating compressive and tensile strain on the atoms along the twin boundary plane. Segregation of Gd and Zn to the twin boundaries was reported by Nie et al. [56], where Gd and Zn solute atoms segregate along twin boundaries, when a compressed Mg1Gd0.5Zn (at%) alloy was heat treated at 150 °C for 3 h. This was observed with advanced transmission electron microscopy techniques. They further reported that twins were stable following heat treatment of Mg0.2Gd (at%) alloy after annealing at 300 °C for 20 min, while such twins were not stable in Mg0.4Zn (at%) alloy after similar thermal treatments.

A recent observation by Zeng et al. [57] found in Mg-0.3Zn-0.1Ca (at%) alloys, following deformation at room temperature and annealing at 350 °C for 15 min, Ca and Zn segregated to the grain boundaries. They observed that both Mg-0.1Ca (at%) and Mg-0.3Zn-0.1Ca (at%) alloys retained the twinned microstructure and retarded recrystallization during annealing for up to 15 min at 350 °C, but the reasons behind the retention of twinning during annealing and retardation of recrystallizations is not clear. It has been reported that Y and Ca have similar effects in Mg terms of texture modification as observed for Gd in Mg [58,59].

As Ca and Y are both larger atoms similar to Gd or Nd, it is likely that Ca or Y and Zn atoms segregate to the twin boundaries during deformation and stabilize the twin boundaries preventing recrystallization. Even though Nie et al. [56] and Zeng et al. [57] illustrate what happens during annealing of deformed microstructures, the question, whether the same process occurs during hot compression at 350 °C, remains unclear and needs to be clarified further.

5 Conclusions

The evolution of the microstructure changes during compression was investigated with in situ synchrotron radiation diffraction for as-cast specimens of ZK40, ZK40-2CaO and ZK40-1Y at 350 °C, and results reveal that the deformation mechanisms differ between the ZK40 and the ZK40 alloys with CaO or Y additions. From the results the following conclusions can be drawn:

- Continuous dynamic recrystallization is observed during compression for ZK40, exhibited in the AT-plot by the blurring of the timelines.
- Continuous and discontinuous dynamic recrystallization occurs during the deformation in the ZK40-2Y alloy, evidenced by the presence of sub-grains and new grains at the grain boundary. On the other hand, dynamic recrystallization was not pronounced for the ZK40-2CaO alloy.
- The influence of the intermetallic compounds in pinning the grain boundary, hampering grain sliding, caused more significant changes in terms of the mechanical behaviour for ZK40-1Y alloy than for the ZK40-2CaO alloy, which can be attributed to the strength of each intermetallic compound.
- The increased yield and maximum strength for the ZK40-1Y alloy can be explained by the presence of intermetallic particles. The surprisingly similar behaviour between the ZK40 alloy and ZK40-2CaO alloy can be attributed to the low strength of the intermetallic particles that were distributed along the grain boundaries of the ZK40-2CaO alloy.

Acknowledgments

The authors acknowledge the Deutsches Elektronen-Synchrotron for the provision of facilities within the framework of proposal I-20130434. RHB acknowledges University of São Paulo for granting the fellowship 'Bolsa Empreendedorismo'.

References

1. M. Perkguleryuz, K. Kainer, A. Kaya, Fundamentals of Magnesium Alloy Metallurgy, 1st ed., Woodhead, Philadelphia, 2013.
2. Z. Yang, J.P. Li, J.X. Zhang, G.W. Lorimer, J. Robson, Review on research and development of magnesium alloys, Acta Metall. Sin. (English Letters) 21 (2008) 313–328.

3. M.K. Kulekci, Int. J. Adv. Manuf. Technol. 39 (2008) 851–865.

4. C.H. Cáceres, Mater. Des. 30 (2009) 2813–2822.

5. M.M. Avedesian, H. Baker, Magnesium and magnesium alloys, in: ASM Speciality Handbook, ASM International, Metal Park, OH, 1999.

6. M.H. Yoo, J.R. Morris, K.M. Ho, S.R. Agnew, Metall. Mater. Trans. A 33 (2002) 813–822.

7. H.J. McQueen, E. Evangelista, J. Bowles, G. Crawford, Met. Sci. 18 (8) (1984) 395–402.

8. S.E. Ion, F.J. Hunphreys, S.H. White, Acta Metall. 30 (1982) 1909–1919.

9. Z. Ya, Z. Xiaoqin, L. Chen, D. Wenjiang, Mater. Sci. Eng. A 428 (2006) 91–97.

10. A. Galiyev, R. Kaibyshev, G. Gottstein, Acta Mater. 49 (2001) 1199–1207. [11] E.I. Poliak, J.J. Jonas, Acta Mater. 44 (1996) 127–136.

11. L. Shubo, W. Yanqiu, Z. Mingyi, W. Kun, Trans. Nonferrous Met. Soc. 14 (2004) 306–310.

12. S.M. He, L.M. Peng, X.Q. Zeng, W.J. Ding, Y.P. Zhu, Mater. Sci. Eng. A 433 (2006) 175–181.

13. T. Homma, C.L. Mendis, K. Hono, S. Kamado, Mater. Sci. Eng. A 527 (2010) 2356–2362.

14. S.-Y. Chang, H. Tezuka, A. Kamio, Mater. Trans. 38 (1997) 526–535.

15. Y. Wu, H. Yan, S. Zhu, J. Chen, A. Liu, X. Liu, T. Nonferr, Metal. Soc. 24 (2014) 930–939.

16. J. Hofstetter, S. Rüedi, I. Baumgartner, H. Kilian, B. Mingler, E. Oovoden-Karadeniz, S. Pogatscher, P.J. Uggowitzer, J.F. Löffler, Acta Mater. 98 (2015) 423–432.

17. T.Y. Kwak, H.K. Lim, W.J. Kim, Mater. Sci. Eng. A 648 (2015) 145–156.

18. A.A. Luo, Int. Mater. Rev. 49 (2004) 13–30.

19. A. Suzuki, N.D. Saddock, J.R. Terbush, B.R. Powell, J.W. Jones, T.M. Pollock, Metall. Mater. Trans. A 39 (2008) 696–702.

20. Y. Chino, T. Ueda, Y. Otomatsu, K. Sassa, X. Huang, K. Suzuki, M. Mabuchi, Mater. Trans. 52 (2011) 1477–1482.

21. B. Zhang, Y. Wang, L. Geng, C. Lu, Mater. Sci. Eng. A 539 (2012) 56–60.

22. S.-H. Ha, J.-K. Lee, H.-H. Jo, S.-B. Jung, S.K. Kim, Rare Met. 25 (2006) 150–154.

23. B. Wiese, C.L. Mendis, D. Tolnai, A. Stark, N. Schell, H.-P. Reichel, R. Brückner, K. U. Kainer, N. Hort, J. Alloy. Compd. 618 (2015) 64–66.

24. K. Oh-ishi, R. Watanabe, C.L. Mendis, K. Hono, Mater. Sci. Eng. A 526 (2009) 177–184.

25. C.J. Bettles, M.A. Gibson, K. Venkatesan, Scr. Mater. 51 (2004) 193–197.

26. X. Gao, S.M. Zhu, B.C. Muddle, J.F. Nie, Scr. Mater. 53 (2005) 1321–1326.

27. L. Katsarou, K. Suresh, K.P. Rao, N. Hort, C. Blawert, C.L. Mendis, H. Dieringa, Magnes. Technol. 2015 (2015) 419–423.

28. T.Y. Kwak, W.J. Kim, Mater. Sci. Eng. A 615 (2014) 222–230.

29. S. Yoshimoto, M. Yamasaki, Y. Kawamura, Mater. Trans. 47 (2006) 959–965.

30. A. Singh, M. Watanabe, A. Kato, A.P. Tsai, Mater. Sci. Eng. A 385 (2004) 382–396.

31. D.K. Xu, L. Liu, Y.B. Xu, E.H. Han, Mater. Sci. Eng. A 443 (2007) 248–256.

32. Y. Chino, S. Kensuke, M. Mabuchi, Mater. Sci. Eng. A 513 (2009) 394–400.

33. D.K. Xu, L. Liu, Y.B. Xu, E.H. Han, J. Alloy. Compd. 426 (2006) 155–161.

34. S.A. Farzadfar, M. Sanjari, I.-H. Jung, E. Essadiqi, S. Yue, Mater. Sci. Eng. A 528 (2011) 6742–6753.

35. S.R. Agnew, M.H. Yoo, C.N. Tomé, Acta Mater. 49 (2001) 4277–4289.

36. S. Sandlöbes, M. Friák, S. Zaefferer, A. Dick, S. Yi, D. Letzig, et al., Acta Mater. 60 (2012) 3011–3021.

37. N. Stanford, R. Cottam, B. Davis, J. Robson, Acta Mater. 78 (2014) 1–13.

38. K.-D. Liss, U. Garbe, H. Li, T. Schambron, J.D. Almer, K. Yan, Adv. Eng. Mater. 11 (2009) 37–40.

39. K.-D. Liss, K. Yan, Mater. Sci. Eng. A 528 (2010) 11–27.

40. K.-D. Liss, T. Schmoelzer, K. Yan, M. Reid, R. Dippenaar, H.J. Clemens, Appl. Phys. 106 (2009) 044914–044916.

41. T. Schmoelzer, K.-D. Liss, P. Staron, S. Mayer, H. Clemens, Adv. Eng. Mater. 13 (2011) 685–699.

42. I. Lonardelli, N. Gey, H.-R. Wenk, M. Humbert, S.C. Vogel, L. Lutterotti, Acta Mater. 55 (2007) 5718–5727.

43. P. Suwanpinij, A. Stark, X. Li, F. Römer, K. Herrmann, T. Lippmann, W. Bleck, Adv. Eng. Mater. 15 (2014).

44. K.-D. Liss, K. Yan, M. Reid, Mat. Sci. Eng. A 601 (2014) 78–85.

45. K. Yan, K.-D. Liss, U. Garbe, J. Daniels, O. Kirstein, H. Li, R. Dippenaar, Adv. Eng. Mater. 11 (2009) 771–773.

46. K. Yan, D.G. Carr, M.D. Callaghan, K.-D. Liss, H. Li, Scr. Mater. 62 (2010) 246–249.

47. F.R. Elsayed, N. Hort, M.A. Salgado-Ordorica, K. Kainer, Mater. Sci. Forum 690 (2011) 65–68.

48. Test Methods for Determining Average Grain Size, (n.d.), doi: ?http://dx.doi.org/10.1520/e0112-96r04-02?.

49. D. Tolnai, G. Szakacs, G. Requena, A. Stark, N. Schell, K. Kainer, N. Hort, Mater. Sci. Forum 765 (2013) 286–290.

50. J. Bettles, M. Barnett, Advances in Wrought Magnesium Alloys: Fundamentals of Processing Properties and Applications, Woodhead Publishing, Oxford, 2012.

51. R.E. Reed-Hill, E.P. Dahlberg, W.A. Slippy, Trans. AIME 233 (1965) 1766–1771.

52. S.R. Agnew, M.H. Yoo, C.N. Tome, Acta Mater. 49 (2001) 4277–4289.

53. L. Capolungo, I.J. Beyerlein, C.N. Tomé, Scr. Mater. 60 (2009) 32–35.

54. A. Ostapovets, R. Gröger, Model. Simul. Mater. Sci. Eng. 22 (2014) 025015.

55. J.F. Nie, Y.M. Zhu, J.Z. Liu, X.Y. Fang, Science 340 (2013) 957–960.

56. Z.R. Zeng, Y.M. Zhu, M.Z. Bian, C.H.J. Davies, N. Birbilis, J.F. Nie, Acta Mater. 105 (2016) 479–494.

57. T. Laser, C. Hartig, M.R. Nürnberg, D. Letzig, R. Bormann, Acta Mater. 56 (2008) 2791–2798.

58. Y. Chino, T. Ueda, Y. Otomatsu, K. Sassa, X. Huang, K. Suzuki, M. Mabuchi, Mater. Trans. 52 (2011) 1477–1482.